A detailed investigation of the structural stability, ionic conductivity and *in situ* δ-phase formation of $Y_xBi_{2-x}O_3$

Mathias A. Kiefer[1,3] iD, **Caren Billing**[1*] iD, **Rudolph M. Erasmus**[2,3] iD, **Wilson M. Mogodi**[4] iD **and David G. Billing**[1,3] iD

[1]Molecular Science Institute, School of Chemistry, University of the Witwatersrand, Private Bag X3, Johannesburg, 2050, South Africa.
[2]Material Physics Research Institute and Microscopy and Microanalysis Unit, University of the Witwatersrand, Private Bag X3, Johannesburg, 2050, South Africa.
[3]DSI-NRF Centre of Excellence in Strong Materials, University of the Witwatersrand, Private Bag X3, Johannesburg, 2050, South Africa.
[4]Centre for Supramolecular Chemistry Research, Department of Chemistry, University of Cape Town, Rondebosch, Cape Town, South Africa.

ABSTRACT
The *in situ* δ-phase formation for a series of yttrium-doped Bi_2O_3 materials was studied by Raman spectroscopy and high resolution X-ray diffraction under variable temperature conditions. Contrary to previous reports, for dopant concentrations less than 25%, the cubic δ-phase was not fully stabilized at room temperature – tetragonal phase content was evident in both Raman spectra and powder diffractograms. Arrhenius plots also showed evidence of a phase transformation by the distinct large step change in conductivity in the temperature region where the tetragonal-cubic phase transformation was noted. Both the thermal expansion and ionic conductivity of the cubic phase decreased with increasing dopant content.

INTRODUCTION

The δ-phase of Bi_2O_3 shows both immense promise and a multitude of limitations as a solid oxide electrolyte. It is the highest oxide ion conducting material known, with conductivities around 1 S.cm^{-1} at 750 °C.[1–3] The reasons for this spectacularly high conduction have been elegantly summarized by Boivin and Mairesse:[4] (i) 25% of the oxygen sites are vacant in the fluorite-type lattice, (ii) Bi^{3+} has an electronic structure characterized by the presence of a $6s^2$ lone pair of electrons which leads to high polarizability of the cation network and (iii) Bi^{3+} has the ability to accommodate highly disordered surroundings. It has further been shown via neutron diffraction studies that in these Fmm-structured oxides, oxide ions are disordered across the 8c sites and the 32f sites[5,6] (as indicated in Figure 1). Neutron total scattering studies have indicated the occupancy of an additional 48i site which further adds to the highly disordered nature of this structure.[7] Furthermore, studies by Abrahams et al.[8] and Borowska-Centkowska et al.[9] have shown distinct relationships between the local, defect structure of Bi_2O_3 materials and physical properties such as oxide ion conductivity and thermal expansion.

Although the conductivity of the δ-phase of Bi_2O_3 is orders of magnitude higher than that commonly found for the commercial yttria stabilized zirconia (YSZ) electrolyte materials (between 0.01–0.1 S.cm^{-1} within the temperature range of 700–1000 °C),[10–14] this phase is only stable within a narrow temperature range (730–824 °C) and is characterized by a large coefficient of thermal expansion (CTE) reported between 24.0–43.6 10^{-6} K^{-1}.[15,16] Previous studies have focused on stabilizing the δ-phase to lower temperatures by the addition of lanthanide and transition metal dopants to Bi_2O_3.[15–22] These approaches have been largely successful, with the δ-phase being stabilized to lower temperatures and in some cases, to room temperature. The presence of these dopants in the δ-phase is, however, at the expense of conductivity.[15, 18,23] Remarkably, the effect of doping on the CTE of these stabilized δ-phases is poorly reported, if at all.

This work focuses on using Y^{3+} as the dopant to stabilize the δ-phase.

While the Y^{3+} dopant content required to stabilize the δ-phase has been previously investigated, the exact dopant range to achieve this remains questionable. Previous studies by Takahashi et al.[24] indicated δ-phase stabilization with Y^{3+} content between 25–43 mol% whereas Kale et al.[19] indicated that the δ-phase was stabilized over a broad composition range of 10–40 mol% Y^{3+}. Additional studies have shown that Y^{3+} content greater than 20 mol%[6,25–29] readily stabilizes the δ-phase to room temperature. A more recent study by Liu et al.[30] has shown that the δ-phase is stabilized to room temperature with Y^{3+} content as low as 15 mol%. There seems to be agreement that δ-phase stabilization occurs for Y^{3+} content above 20–25 mol%, but the question remains as to whether the δ-phase is truly stabilized with Y^{3+} content below 20 mol%, and especially as low as 10–15 mol%. This issue is raised here due to peak asymmetry noted in the diffraction pattern for the sample containing 10 mol% Y^{3+} in the work published by Takahashi et al.[24], although they did not comment on this. In the study by Liu et al.[30] peak asymmetry for the 10 mol% Y^{3+} was also noted and at this dopant level a cubic and tetragonal phase mixture is reported. This asymmetry was not noted for samples containing 15–25 mol% Y^{3+}. The pattern for the 10 mol% Y^{3+} composition was unfortunately omitted in the study by Kale et al.[19]

A citrate sol–gel synthetic route was employed here since it is faster and requires less energy when compared to the conventional solid state methods generally used in literature. The sol–gel method also ensures homogenous mixing of reactants from the start while still in the solution state. The amount of Y^{3+} used to stabilize the δ-phase was investigated with the aim to establish the dopant range in which the δ-phase is truly stabilized on synthesis. The relationship between the dopant percentage and its effect on conductivity and δ-phase thermal expansion was studied, along with the *in situ* δ-phase formation.

MATERIALS AND METHODS

Synthesis and sample preparation

All samples were prepared by means of a citrate sol–gel process[31]. Stoichiometric amounts of bismuth nitrate pentahydrate ($Bi(NO_3)_3.5H_2O$, 99.99% pure, Aldrich) and yttrium nitrate

*To whom correspondence should be addressed
Email: caren.billing@wits.ac.za

hexahydrate ($Y(NO_3)_3.6H_2O$, 99.8% pure, Aldrich) were dissolved in glacial acetic acid (98% pure, MK Chemical, 99%) under moderate heating and stirring. Aqueous solutions were avoided as far as possible to prevent the precipitation of Bi^{3+} hydrolysis products which can form even under acidic conditions.[31] Excess citric acid monohydrate ($C_6H_8O_7.H_2O$, ACS reagent, Aldrich) was added and the resulting mixture evaporated to form a metal complex paste. Finally, the dried precursor was calcined at 450 °C for 18 h to obtain the $Y_xBi_{2-x}O_3$ powders and a portion of the sample was used for the *in situ* δ-phase formation studies by powder X-ray diffraction (PXRD) and Raman spectroscopy. The rest of the sample was ground into a fine powder using an agate mortar and pestle and then annealed at 750 °C for 8 h for further analysis by PXRD. A range of samples were prepared with varying dopant concentration, with samples having relatively high dopant concentrations (25 and 27.5 mol% Y^{3+}) which are known to be δ-phase stabilized and those with lower dopant concentrations (10–22.5 mol% Y^{3+}) which are the samples of interest. For ease of referring to the various samples, a 10% Y_2O_3 doped Bi_2O_3 sample is called 10YSB (yttria stabilized bismuth oxide) and so on.

Pellets were prepared for impedance studies by mixing the powders annealed at 750 °C with a 2% polyvinyl alcohol solution (as a binder) and dried at 120 °C for 20 min. This was then uniaxially pressed at 110 MPa into pellets using a 13 mm diameter die to produce pellets of ~1.2 mm thickness. The pellets were heated at 250 °C for 4 h to remove the binder and then sintered at 750 °C for 4 h.

Raman spectroscopy

A Horiba LabRam HR Raman spectrograph coupled to a Lexel Argon ion laser tuned to 514.5 nm and a Linkham TS1500 sample stage were used to collect *in situ* variable-temperature Raman spectra. Spectra were collected at 170 °C intervals with an approximate dwell time of 10 minutes in the range of 19–850 °C applying a heating rate of 10 °C min^{-1}.

Powder X-ray diffraction

Room temperature powder X-ray diffractograms were collected on a Bruker D2 Phaser using iron filtered CoK_α radiation (λ = 1.788 Å). High resolution powder diffractograms of selected calcined (at 450 °C) samples were also collected *in situ* at beamline ID22 (λ = 0.3544 Å) at the European Synchrotron Radiation Facility (ESRF). Samples were loaded into quartz capillaries and the temperature raised using a hot-air blower. Diffractograms were collected at ~50 °C intervals from room temperature to 769 °C, with the set temperatures corrected according to the facilities temperature calibration profile. For easier comparison of diffractograms measured using different wavelength X-rays, the intensities were plotted against the momentum transfer (Q) rather than 2θ as is commonly done, where Q = {4π sin(2θ/2)}/λ. Phase identification of diffractograms was done using Bruker AXS DIFFRAC.EVA V4.2 linked to the crystallography open database (COD).[32] Rietveld refinement of the diffractograms was done using Bruker AXS TOPAS-Academic Version 6.[33] In the refinements of the lab-based diffractograms collected at room temperature, the instrument resolution function (IRF)[34] was determined using NIST 660a and was described using the fundamental parameters approach[35] using the full axial divergence model[36] to account for divergence-related asymmetry of the diffraction peaks and source emission profile. In the refinements of the synchrotron *in situ* diffractograms, the IRF was determined using NIST 640d and was described using the Thompson Cox Hastings (TCHZ) Pseudo-Voight function[37] with the divergence-related asymmetry effects described in an empirical way using the simple axial model.[34] In each refinement, the parameters refined were the scale factors, selected corrections, and lattice parameters. Furthermore, the compositional stoichiometry for the samples were fixed, atomic positional parameters were fixed to those published for the respective crystal structures, and atomic thermal parameters were

fixed to reasonable values. The primary results from the refinements of the samples studied as well as the NIST standards used for instrument calibration are included as Supporting Information.
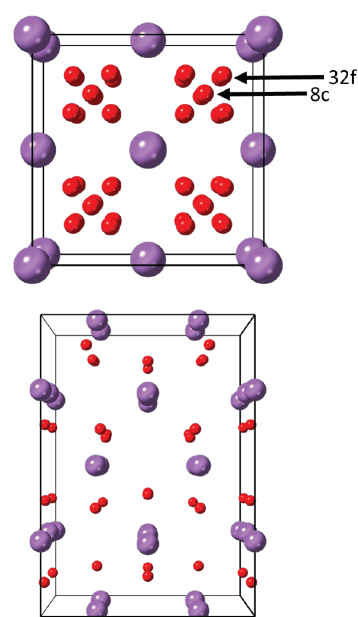
Electrochemical impedance spectroscopy

Impedance of the sintered pellets was measured using a BioLogic MTZ-35 frequency response analyzer interfaced to a computer running MT-Lab software version 1.21. This was coupled to a BioLogic HTF-1100 furnace and a HTSH-1100 sample holder were employed. The additional system impedances were compensated for prior to measuring the impedance of the samples. A frequency range of 0.1 Hz to 1 MHz and an amplitude of 10 mV was employed. The measurements were taken in steps of 50 °C within the range 300–750 °C, with a 30 min dwell time per step. The sample holder contains of two platinum discs, a similar diameter to the sample, between which the pellet is placed and the spring-loaded system in then tightened. No additional coatings were used on the pellet. Thus, each pellet was measured using two consecutive heating and cooling cycles. The Nyquist plots were modelled via an equivalent circuit approach using EC-Lab version 11.21. Ionic conductivities (σ) of the materials were calculated over the temperature range studied using σ = $L/(R1\ A)$, where L is the thickness of the pellet, R1 is the total electrolyte resistance derived from the equivalent circuit modelling or directly from the Nyquist plot (as described in Section 3.3), and A is the surface area of the pellet.

RESULTS AND DISCUSSION

In situ investigation of the δ-phase formation using Raman spectroscopy

The cubic (δ) and tetragonal (β) bismuth oxide structures (Figure 1) have inherently different Bi-O bond lengths and bond strengths which leads to different sets of Raman spectral features thus allowing the discrimination between these two structures. This was clearly shown in the study by Hardcastle and Wachs.[38] The tetragonal structured material produced three prominent bands corresponding to Bi-O stretches at 462, 311 and 124 cm^{-1} indicating a distorted octahedral

Figure 1: Unit cells for the face-centered cubic δ-phase (top) and the tetragonal β-phase (bottom) of bismuth oxide. Purple and red spheres represent the cation and anion sites, respectively. The δ-phase, a defect fluorite phase, is shown with all the possible 8c and 32f oxide positions.[7]

arrangement. The cubic structure (obtained by doping with Nb^{5+} or Ta^{5+})[38] gave two broad bands at 550 and 320 cm^{-1} which were similarly assigned to Bi-O stretches in BiO_5 polyhedra. Group theory calculations, however, predict that the defect fluorite (Fmm) structure should only have one Raman-active mode corresponding to $\Gamma = F_{2g}$ for BiO_6 octahedra.[39] Subsequent studies have clearly shown the presence of a single band at ~630 cm^{-1} for the cubic δ-phase.[29,40] This band is generally broad due to the large extent of disorder. Prominent bands below 200 cm^{-1} are assigned to external lattice vibrations and thus were not further analyzed.
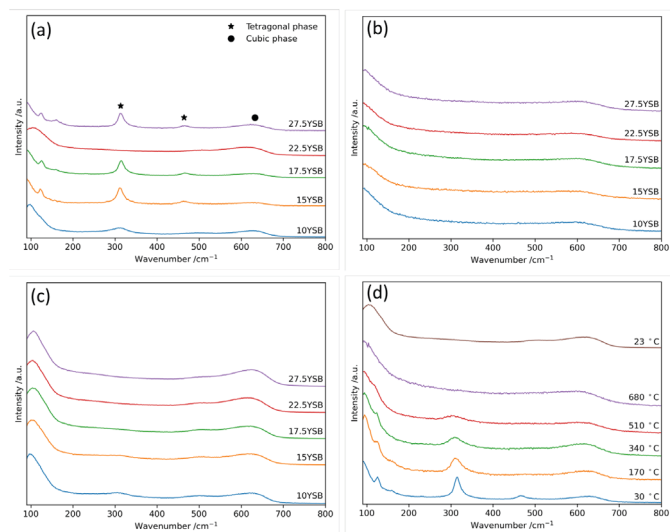
The room temperature Raman spectra collected of the samples that were simply calcined at 450 °C (Figure 2a), indicate the presence of both the tetragonal and cubic phases. The apparent absence of the tetragonal phase for the 22.5YSB sample at room temperature is most likely due to the small sampling area and indicates sample inhomogeneity typical of phase mixtures. For spectra measured at 680 °C (Figure 2b), the bands reflecting the tetragonal phase had disappeared for all doping ranges indicating a conversion to the cubic defect fluorite phase. On cooling back to ~30 °C (Figure 2c) for the low dopant samples (10-15YSB), the reappearance of the most prominent peak for the tetragonal phase (at 311 cm^{-1}) indicated that the cubic phase was not fully stabilized. Figure 2d gives an example of an overall *in situ* heating experiment for the 17.5YSB sample demonstrating that the tetragonal phase is converted to the cubic phase somewhere between 510 and 680 °C. As expected, the Raman signal intensity decreases with increasing temperature.

The higher intensity of the peak indicating the cubic phase in the spectra collected after cooling (at ~30 °C) is most likely due to number of factors, including the increased cubic phase content as well as increased crystallinity caused by heating the sample.
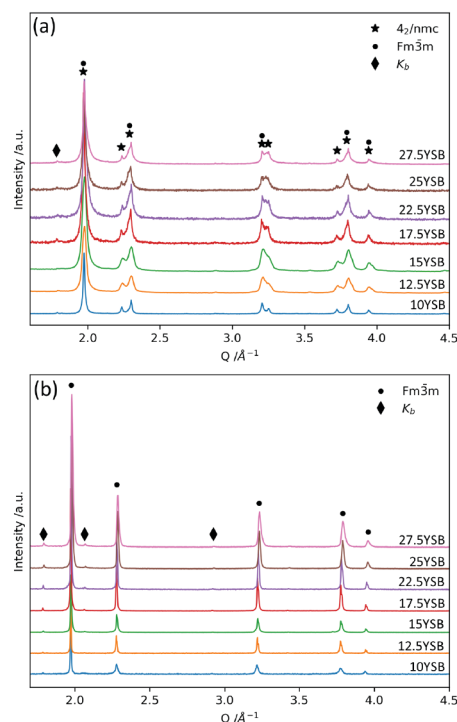
An unexplained observation is the appearance of a low intensity diffuse band at ~500 cm^{-1} for all samples upon cooling (Figure 2c) after the heating cycle. This is most likely due to the formation of an unidentified phase and not due to the disordering of the structure or the change in the number of oxygen vacancies.[29]

Ex situ and *in situ* investigations of the δ-phase formation using powder X-ray diffraction

As was observed from the Raman spectra (Figure 2a), the diffraction patterns of all samples calcined at 450 °C exhibited a mixture of the tetragonal (4_2/nmc, SG #137) and cubic (Fmm, SG #225) phases

Figure 3: Room temperature diffractograms of the series YSB samples (a) calcined at 450 °C indicating mixtures of the tetragonal and cubic phases for all materials and (b) subsequently annealed at 750 °C showing all materials to predominantly consist of the cubic phase.

(Figure 3a). From this data, which gives the average structure, the tetragonal phase is clearly present for the 22.5YSB sample. This corroborates that the apparent missing bands for the tetragonal phase for this sample (Figure 2a) are due to sample inhomogeneity.

Rietveld refinements of these mixtures yielded key structural information for both phases (Table 1, Figure S3 and Table S2). This showed that there were no correlations between the unit cell volume and the dopant percentage when a mixture of phases was present. The significant overlap of tetragonal and cubic phase peaks, coupled with the limited resolution of the lab diffractometer, results in a degree of uncertainty in the reported lattice parameter values for the mixed phase materials. Additionally, the tetragonal phase content of the

Figure 2: Raman spectra of the series of YSB samples calcined at 450 °C collected at (a) room temperature (~23 °C) prior to undergoing any heating, (b) 680 °C during *in situ* heating and (c) upon cooling (~30 °C) after undergoing *in situ* heating measurements. A full variable temperature run is shown for 17.5YSB in (d).

Table 1: Variation of the phase composition (weight %) and cell parameters in the series of YSB materials. Values are given for both the tetragonal and cubic phases for the calcined samples, and for the dominant cubic phase for the annealed samples.
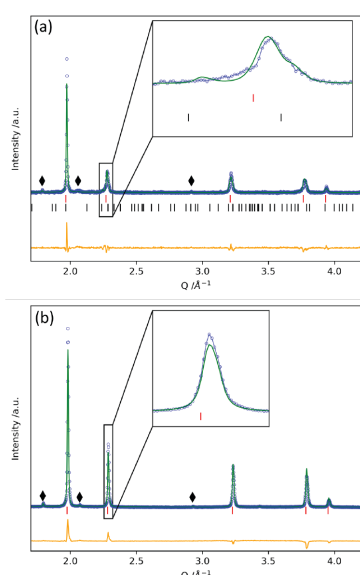
Sample	Calcined at 450 °C				Annealed at 750 °C	
	Tetragonal phase		Cubic phase		Cubic phase	
	a /Å	c /Å	a /Å	Phase %	a /Å	Phase %
10YSB ($Bi_{1.8}Y_{0.2}O_3$)	7.744 (5)	11.270 (6)	5.522 (3)	30.7	5.536 (5)	60.3
12.5YSB ($Bi_{1.75}Y_{0.25}O_3$)	7.748 (7)	11.249 (20)	5.503 (4)	34.3	5.525 (5)	69.4
15YSB ($Bi_{1.7}Y_{0.3}O_3$)	7.745 (11)	11.258 (26)	5.511 (15)	42.9	5.522 (2)	76.1
17.5YSB ($Bi_{1.65}Y_{0.35}O_3$)	7.744 (9)	11.264 (18)	5.508 (7)	61.8	5.518 (1)	92.9
22.5YSB ($Bi_{1.55}Y_{0.45}O_3$)	7.750 (9)	11.269 (7)	5.511 (6)	75.4	5.512 (1)	98.6
25YSB ($Bi_{1.5}Y_{0.5}O_3$)	7.750 (12)	11.261 (23)	5.503 (8)	78.9	5.505 (1)	100
27.5YSB ($Bi_{1.45}Y_{0.55}O_3$)	7.744 (7)	11.261 (15)	5.498 (5)	80.8	5.500 (3)	100

mixture significantly decreased with increasing dopant content. This indicates that higher dopant percentages favor cubic phase formation at lower temperatures.
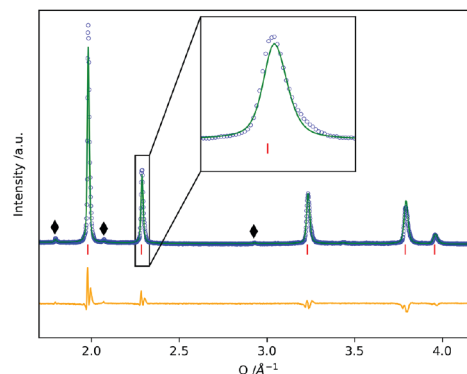
After further annealing these mixtures at 750 °C for 8 h, it is shown that the tetragonal phase readily converted to the cubic phase (Figure 3b). However, on more critical analysis of the diffractograms, significant peak asymmetry and peak broadening was observed for the 10-22.5YSB samples, as revealed in Figure 4a for 10YSB. These features are indicative of tetragonal phase content,[30,41] which is in line with the results from the Raman spectra measured at ~30 °C upon cooling after the heating cycle (Figure 2c). The phase content was quantified using Rietveld refinement (Table 1, Fig S4 and Table S3), and as expected, the tetragonal phase content shows a decrease with increasing dopant percentage. No tetragonal phase was detected above 22.5% Y[3+] content as depicted in Figure 4b for 25YSB. This shows that significantly higher Y[3+] content is required to stabilize the cubic phase than previously reported.[19,30] This again indicates that higher dopant percentages promote cubic phase purity, as was observed for the series of calcined samples (Table 1). Furthermore, for the largely phase pure samples the lattice parameter decreased linearly with increasing dopant percentage (Table 1), as predicted by Vegard's law.[42]

Interestingly, for the 27.5YSB sample there also exists some peak asymmetry (Figure 5) which is not related to the tetragonal phase. This could be indicative of either microstructural defects or an unidentified secondary phase (as was alluded to by the formation of a Raman band at ~500 cm^{−1} for all samples in Figure 2c). Further analysis of this anomaly is a key topic of ongoing work.
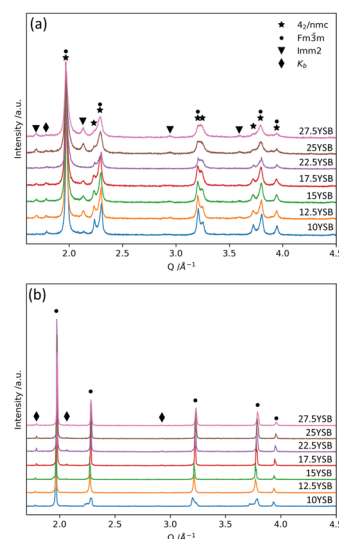
Spontaneous room temperature phase transformations of these materials occur which are more pronounced for the low dopant samples and is the topic of as yet unpublished work. Therefore, samples were remade to perform impedance measurements to ensure no phase aging effects contribute to the electrochemical measurements. Unexpectedly a bismuth sub-carbonate phase (Imm2, SG #44) was additionally detected in the calcined materials (Figure 6a) despite following the same procedure as before. In this case a bismuth sub-carbonate phase (Imm2, SG #44) was additionally detected in the calcined materials (Figure 6a). This phase arises from the initial presence of citrate which is driven off during the calcination step as CO_2. The incomplete

Figure 5: Diffractogram of the 27.5YSB sample annealed at 750 °C having been analyzed by means of Rietveld refinement. The color coding is as for Figure 4 and the inset highlights the mismatch between the observed and calculated patterns due to peak asymmetry. K_β reflections are labelled with diamond markers.
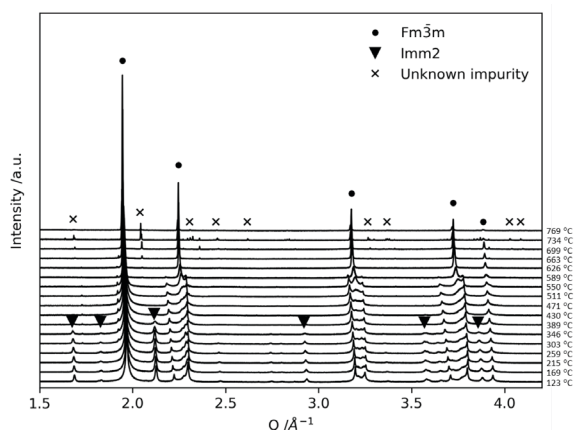

Figure 6: Room temperature diffractograms of a second series YSB samples (a) calcined at 450 °C and (b) subsequently annealed at 750 °C.

calcination appears to form a sub-carbonate phase which is then fully converted upon annealing at 750 °C (Figure 6b).

The phase content was again quantified for both the calcined and annealed samples using Rietveld refinement (Figs. S5,S6 and Tables S4,S5) and similar trends in the lattice parameters were observed. Of interest here is that the phase purity of the final annealed samples. For the 15-27.5YSB materials, the phase purity was reproducible between the first and second series of materials made. The 10YSB and 12.5YSB samples, however, showed reduced cubic phase purity (being 35.2 and 57.3%, respectively for this batch). This variation in cubic phase purity attributed to the presence of the sub-carbonate phase which is found to reduce cubic phase formation for low dopant content samples in yet unpublished work.

The average crystallite size for both batches of samples was ~185 nm, as derived from the PXRD Rietveld refinements. The sizes reported for powder Bi_2O_3 by Anilkumar et al.[43] (who also used the citrate sol–gel synthetic process) was ~100 nm from PXRD and ~50 nm from TEM. Tsuji et al.[44] (who used the conventional solid state synthetic method) reported a crystallite size of ~70 nm for yttrium doped Bi_2O_3 powder from PXRD Rietveld refinements. The solid state synthetic method requires far more grinding of samples and hence it is not surprising that the crystallite size is smaller in this case.

Samples of selected compositions were again remade and calcined at 450 °C as before for *in situ* studies at ID-22 at the ESRF

Figure 4: Diffractograms showing Rietveld refinement analysis for (a) 10YSB and (b) 25YSB, both annealed at 750 °C. The observed pattern is shown in blue, the calculated in green and the difference in orange. Miller indices corresponding to the cubic and tetragonal phases are shown with red and black ticks, respectively. The inset in (a) accentuates the peak asymmetry contribution from the presence of the tetragonal phase. K_β reflections are labelled with diamond markers.

Figure 7: *In situ* diffractograms of the 17.5YSB sample calcined at 450 °C collected at ~40 °C intervals over the temperature range of 123–769 °C.

Table 2: Comparison of CTEs determined for materials annealed at 750 °C studied in this work (determined between 589–769 °C) and those reported for currently used SOFC components.

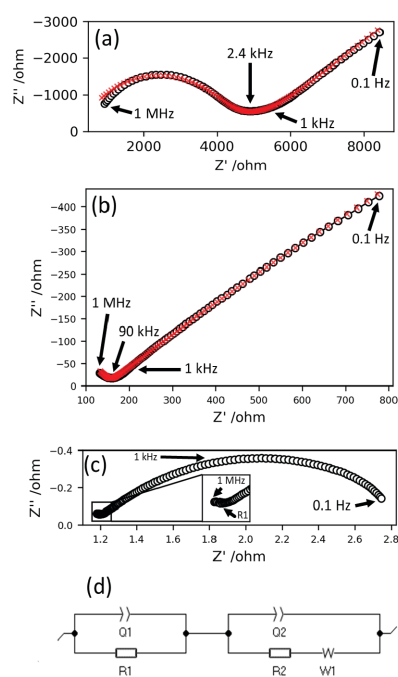| Component	Material	CTE /10⁻⁶ K⁻¹	Reference
		$CTE\ /10^{-6}\ K^{-1}$	
Electrolyte	15YSB	152.4 ± 14.2	This work
Electrolyte	17.5YSB	78.5 ± 11.9	This work
Electrolyte	22.5YSB	27.1 ± 2.5	This work
Electrolyte	20YSB	15.4[a] and 20.3[b]	[29]
Electrolyte	8YSZ	10.5–10.9	[50]
Inter-connect	Ferritic steel, ×10CrAl 18	12.9–13.9	[51]
Cathode	Perovskite, $La_{0.65}Sr_{0.3}MnO_3$	12.0–12.3	[50]
Anode	Cermet, 40 v/o Ni + 60 v/o 8YSZ	12.5-12.6	[51]

[a] *CTE over the temperature range of 30-500 °C*
[b] *CTE over the temperature range of 500-800 °C*

Analysis of conductivity using electrochemical impedance spectroscopy

Electrochemical impedance spectroscopy (EIS), used to determine the conductivity of these types of materials, has also proven to be extremely useful and sensitive in detecting phase changes when measurements are made as a function of temperature. Variable temperature-EIS was thus used to establish whether the extent of cubic phase purity obtained from the analysis of the XRD data was feasible.

Examples of Nyquist plots, as measured using EIS of the pelletized materials (initially annealed and then sintered at 750 °C), are displayed in Figure 8a–c (Figures S15–S20 give the full set of data). In the low temperature region (300-450 °C), data were modelled using the equivalent circuit indicated in Figure 8d. In general, the spectra of all materials, whether it was found to be phase pure or not, displayed a single arc in the high frequency region which was fitted using a Randles circuit with R1 representing the electrolyte resistance. A constant

(Figures S7–S12 and Tables S6–S8). The high resolution PXRD data of 15YSB (Figure S10) and 17.5YSB (Figure 7) clearly showed the predominantly tetragonal starting phase converting into the desired cubic phase upon heating from 123–769 °C (Figure S13). Throughout the heating cycle, impurity phases were present. Here too the bismuth sub-carbonate phase was evident in the diffractograms for 15YSB and 17.5YSB measured from 123–390 °C. By 430 °C the phase was no longer detected which indicates that a calcination temperature of 450 °C should be sufficient and perhaps longer calcination times should rather be implemented. Around 550–626 °C the tetragonal phase disappears. This is in line with the observations made from the *in situ* Raman spectroscopy measurements which showed the tetragonal-cubic phase conversion taking place between 510-680 °C, but also provides a more accurate indication of the temperature range in which this conversion takes place and gives confidence that an annealing temperature of 750 °C is adequate. At higher temperatures trace quantities of unknown impurity metal oxides (likely Y_2O_3) were produced. These impurity phases largely disappeared at 769 °C and were also not prevalent in the *ex situ* samples when longer annealing times were used, however, their formation is noteworthy.

For *in situ* studies of the highly substituted 22.5YSB sample at ID-22, rhombohedral bismuth oxide (Rm, SG #166) is initially present and no tetragonal phase content was detected. The rhombohedral phase was no longer detected by ~663 °C (Figure S9 and S13). The rhombohedral phase was not detected for any composition in both series of YSB materials previously synthesized. This rhombohedral phase is commonly formed when the Bi_2O_3 lattice is doped with large cations[45–47] and is not expected to be present in 22.5YSB based on the dopant radius. However, the rhombohedral phase does form when these materials are annealed for extended periods of time at temperatures below 700 °C.[48,49] This has not been reproduced in other samples of the same composition and hence it is suspected to be due to an inadvertent furnace failure with the set temperature program not necessarily being followed and annealing taking place at a lower temperature.

Between 589–769 °C a predominantly cubic phase was present for the three samples analyzed (Figure S13) and lattice parameter variations, as determined by Rietveld refinement, were employed to the establish the CTEs in this temperature range (Table 2). Wu et al.[29] found the CTE for 20YSB to vary depending on the temperature range studied. In the present work, all cubic phases studied exhibited a linear expansion in the temperature range considered. The CTEs of the YSB moieties were found to dramatically decrease with increasing Y^{3+} content. Even so, for all YSB compositions studied, the rate of thermal expansion was significantly higher than that for the commercially used YSZ electrolyte. This makes these materials unsuitable for application in a typical solid oxide fuel cell (SOFC) due to the immense thermal expansion mismatch with adjacent SOFC components as illustrated in Table 2.

Figure 8: Typical impedance spectra from the second cycle of measurement for 27.5YSB annealed at 750 °C in air at (a) 350 °C and (b) 450 °C with the equivalent circuit fit shown with red markers, and at (c) 750 °C indicating the point where R1 was approximated when modelling was not possible. (d) The equivalent circuit used for modelling data in the 300-450 °C range.

phase element, Q1, was used to model this region indicating that the capacitances were distributed and α1 values ranged from ~0.7–0.8. R1 represents the total electrolyte resistance which incorporates the bulk and grain boundary resistance since they could not be resolved for these polycrystalline materials. Jung and Chung[52] has shown that bismuth oxide materials generally have negligible grain boundary resistance, but this cannot be confirmed here. At higher temperatures (500–750 °C) the data in the high frequency region was insufficient to model, thus the electrolyte resistance was approximated as the real impedance at point R1 indicated in Figure 8c. Bounded diffusion was clearly evident at the high temperatures.

As described in section 2.4, the pelletized sample was sandwiched between two platinum discs thus two consecutive heating and cooling cycles were performed. The temperature dependent conductivity behavior in the form of Arrhenius plots illustrated that the first cycle gave a large hysteresis between heating and cooling (Figure 9). This was not the case for the second cycle, where the results also corresponded to those from the first cooling cycle, thus indicating that the pellet-to-electrode contact was optimized (also see Figure S14). Data from the second cycle thus served as the reported values. Even though this methodology may not produce the optimal conductivities, it is fully sufficient to investigate the extent to which phase changes occur, if at all.
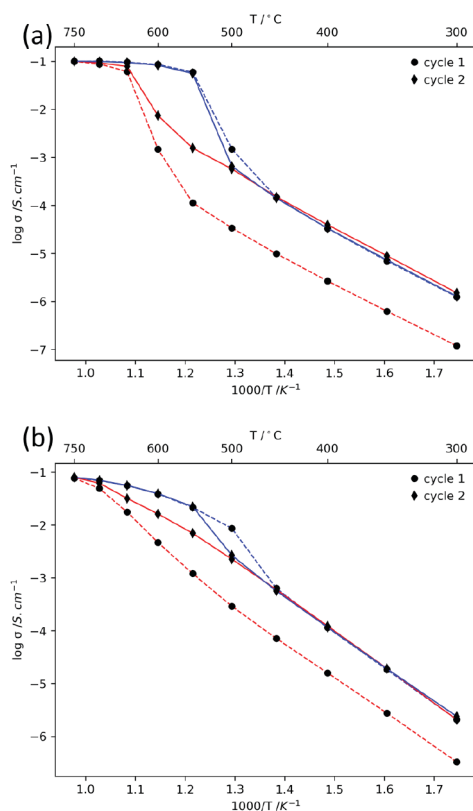
As is expected from a thermally-activated conductivity mechanism that is inherent to ionic conducting ceramics, the conductivities were found to increase on heating and conversely, decrease on cooling. For the low dopant samples (10YSB, 12.5YSB and 15YSB in Figure 10a), it was noted that in the low temperature range, lower conductivities were produced which is clearly due to the presence of the tetragonal impurity phase still present in the annealed (at 750 °C) samples. Additionally, there is a prominent 'step function' type behavior on both the heating and cooling cycles within the temperature range of 550–650 °C. This step is largely attributed to the conversion of the initial phase mixture into a pure cubic phase and the temperature

range in which this occurs corresponds to the *in situ* phase transitions observed in both Raman spectroscopy and high resolution PXRD. The magnitude of this step is also directly related to the extent of the impurity phase present. The Arrhenius plot for 27.5YSB (Figure 10b), found to be a pure cubic phase, was linear until ~500 °C and the ensuing slight 'bend' at higher temperatures is attributed to the order-disorder transition. This order-disorder transition was noted for the low dopant samples after the phase transition step. , The step in the conductivity thus confirms the presence of mixed cubic and tetragonal phases for 10-17.5YSB (Figure 10a and b) as was also determined by the careful analysis of the diffraction patterns. A very small step was observed for 25YSB even though it was found to be 100% pure from XRD refinements. This may reflect the presence of a less conductive phases present in the amorphous fraction of the material.
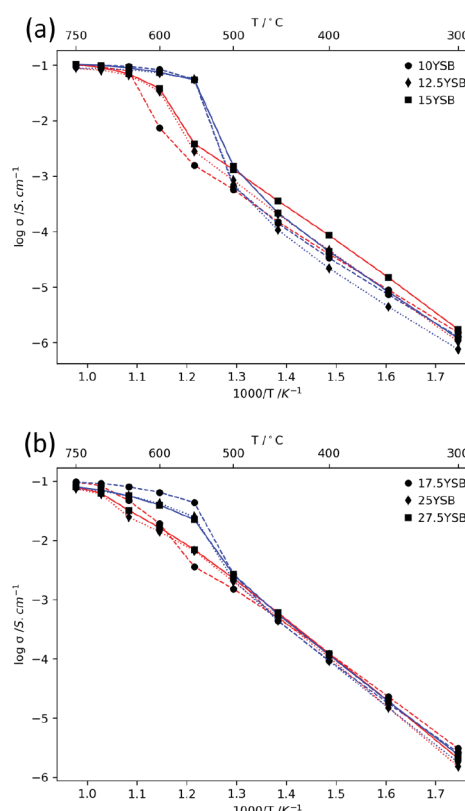
A general trend of increasing activation energy of conduction with increasing dopant concentration was observed (Table 3). The 'step function' type behavior results in a significant reduction in the activation energy at high temperature due to the formation of the

Table 3: Activation energies of YSB materials annealed at 750 °C determined in regions over the temperature range of 300–750–300 °C.

Sample	Activation energy (E_a)			
	over 300–550 °C/eV	over 650–750 °C/eV	over 750–600 °C/eV	over 450–300 °C/eV
10YSB	0.493	0.0889	0.0418	0.486
12.5YSB	0.558	0.102	0.0456	0.511
15YSB	0.545	0.139	0.0730	0.538
17.5YSB	0.504	0.259	0.0896	0.529
25YSB	0.594	0.393	0.128	0.572
27.5YSB	0.576	0.326	0.158	0.567

Figure 9: Arrhenius plots of (a) 10YSB and (b) 27.5YSB materials annealed at 750 °C in the temperature range of 300–750 °C showing results from both the heating (red lines) and the cooling cycles (blue lines) from both measurements cycles.

Figure 10: Arrhenius plots of (a) 10YSB, 12.5YSB, 15YSB and (b) 17.5YSB, 25YSB and 27.5YSB materials (annealed and sintered at 750 °C) showing results from both the heating (red lines) and the cooling cycles (blue lines).

highly conductive cubic phase and the occurrence of an order-disorder transition. However, the very low activation energies observed at high temperatures indicate some electronic conductivity which is unusual for cubic bismuth oxides. This phenomenon is currently under investigation. For the purer samples with higher Y^{3+} content, this feature is significantly less pronounced, if not absent with only minor changes in activation energy during the heating and cooling cycles which are attributed to changes in the ordering of the oxygen sublattice.

Ionic conductivities measured for YSB materials in previous studies are compared to those measured in this work at 600 °C and 750 °C (Table 4). At 750 °C both the 25YSB and 27.5YSB samples have lower conductivities in comparison to those found in previous studies. This discrepancy could be attributed to the different synthetic techniques (with either carbonate coprecipitation[26] or conventional solid state techniques[24,25] previously used) and pellet preparation methodologies used. However, more notable is the application of conductive electrodes, such as Pt, to the pellet surfaces prior to measurement.[24,25] As discussed, in the present work the pellet was sandwiched between two platinum discs of a similar diameter to the sample with no additional coating. Despite using data from the second heating and cooling cycle, this shows that these coatings clearly provide more initmate contact. A difference in measured conductivity is even dependent on the type of coating used, as demonstrated for 22.5YSB in Table 4, with Pt electrodes giving a higher conductivity compared to Ag electrodes.[53] It was also noted that certain conductivity values published for doped bismuth oxides at 750 and 800 °C are questionable since they exceed the benchmark of ~1 S.cm^{-1} at 750 °C for pure Bi_2O_3.[54]

At 600 °C, the 25YSB and 27.5YSB samples exhibited conductivities that are also lower than the literature values on the heating cycle. However, for the cooling cycle the values obtained here are comparable to the literature values. This is due to the higher disordered state maintained on cooling to 600 °C. The state of disorder of the materials hence also affects the measured conductivity and further hinders a comparison to conductivity values found in literature. Therefore, in general, the comparison of the absolute conductivity values is challenging. The trends in the conductivities for a series of materials measured in the same manner, however, reveals very useful information.

Interestingly, markedly higher conductivities were measured at 800 °C. In the present work, measurements at this temperature were not possible due to the lower observed melting point of the materials (~780 °C). This is possibly a result of the synthetic methodology where it could be speculated that features such as microstructure and crystallite size reduce the melting point of the material. Relating the conductivities in this work to that for YSZ and GDC (gadolinium-doped ceria), they were found to be comparable, and in some cases superior, to those at significantly lower temperatures (Table 4).

CONCLUSION

The variable temperature measurements using various techniques shows that the transition from a phase mixture to the δ-phase occurs around ~550–600 °C. This work also clearly shows that the δ-phase is not fully stabilised for the 10-22.5YSB materials and this establishes the dopant range in which the δ-phase is truly stabilized on synthesis. This was confirmed by results obtained from both Raman spectroscopy and PXRD. The assymetry of diffraction pattern peaks that is caused by the presence of secondary phases is often overlooked in laboratory-based experiments.The VT-EIS measurements of these doped YSB materials (which were annealed and sintered at 750 °C) also indicated a phase change in the same temperature range, again reinforcing the presence of a phase mixture at lower temperatures.

By studying a series of YSB samples with varying dopant concentrations, it was seen that with increasing dopant concentration both the CTE and the conductivity decreased. EIS data and subsequent

Table 4: Comparison of the ionic conductivity of YSB materials annealed and sintered at 750 °C studied in this work to that of singly doped electrolytes studied previously.

Composition	Ionic conductivity (σ/S.cm^{-1})					Reference
	600 °C[a]	600 °C[b]	750 °C	800 °C	1000 °C	
10YSB	0.0074	0.083	0.10	–	–	This work
12.5YSB	0.034	0.072	0.088	–	–	This work
15YSB	0.038	0.074	0.10	–	–	This work
17.5YSB	0.019	0.065	0.096	–	–	This work
25YSB	0.014	0.042	0.074	–	–	This work
27.5YSB	0.016	0.039	0.080	–	–	This work
20YSB	0.00525*	–	0.288	0.550	–	[19]
20YSB	0.0251	–	–	–	–	[55]
20YSB	–	–	–	1.97	–	[29]
22.5YSB	0.0193#	–	–	–	–	[53]
22.5YSB	0.0248##	–	–	–	–	[53]
22.5YSB	0.131	–	1.59	2.92	–	[25]
24YSB	0.08	–	–	0.56	–	[27]
25YSB	0.080	–	–	–	–	[24]
25YSB	0.077	–	0.27**	–	–	[26]
25YSB	0.0438	–	0.398	0.631	–	[25]
27.5YSB	0.0490	–	0.380	0.661	–	[25]
30YSB	0.0391	–	0.386	0.649	–	[25]
8YSZ	–	–	–	0.052	0.18	[56]
20GDC	–	–	–	0.096	0.25	[56]

[a] *Conductivity measured during the heating cycle*
[b] *Conductivity measured during the cooling cycle*
* *Conductivity measured at 570 °C*
** *Conductivity measured at 700 °C*
# *Ag electrode painted onto pellet*
Pt electrode painted onto pellet

studies (not presented here) have also indicated that phase aging of the materials occur at room temperature, and is more pronounced for the lower dopant concentrations. This suggests that a comprimise between optimum conductivity, minimal thermal expansion and phase degradation on aging would have to be considered. Based on the findings of this work, for the YSB system we predict that the optimum material for further investigation is 27.5YSB.

From the wide range of conductivies measured for the same dopant concentration, both here and in literature, it can be concluded that the sample preparation and measurement strategies play a significant role in the absolute conductivity value. This is an issue that the community needs to address and provide clearer guidelines so that the results can be more directly compared.

SUPPLEMENTARY MATERIAL

Supplementary information for this article is provided in the online supplement.

ORCID IDs

Mathias A. Kiefer – https://orcid.org/0000-0003-1054-4370
Caren Billing – https://orcid.org/0000-0001-5462-1150
Rudolph M. Erasmus – https://orcid.org/0000-0001-7455-766X
Wilson M. Mogodi – https://orcid.org/0000-0002-3322-2633
David G. Billing – https://orcid.org/0000-0001-8995-924X

REFERENCES

1. Punn R, Feteira AM, Sinclair DC, Greaves C. Enhanced Oxide Ion Conductivity in Stabilized δ-Bi$_2$O$_3$. J Am Chem Soc. 2006;128(48):15386–15387. https://doi.org/10.1021/ja065961d.

2. Cahen HT, Van Den Belt TGM, De Wit JHW, Broers GHJ. The electrical conductivity of δ-Bi$_2$O$_3$ stabilized by isovalent rare-earth oxides R$_2$O$_3$. Solid State Ionics. 1980;1(5-6):411–423. https://doi.org/10.1016/0167-2738(80)90039-9.

3. Laarif A, Theobald F. The lone pair concept and the conductivity of bismuth oxides Bi$_2$O$_3$. Solid State Ionics. 1986;21(3):183–193. https://doi.org/10.1016/0167-2738(86)90071-8.

4. Boivin JC, Mairesse G. Recent Material Developments in Fast Oxide Ion Conductors. Chem. Mater. 1998;10(10):2870–2888. https://doi.org/10.1021/cm980236q.

5. Battle PD, Catlow CRA, Drennan J, Murray AD. The structural properties of the oxygen conducting δ phase of Bi$_2$O$_3$. J. Phys. C Solid State Phys. 1983;16(17):561–566. https://doi.org/10.1088/0022-3719/16/17/003.

6. Battle PD, Catlow CRA, Heap JW, Moroney LM. Structural and dynamical studies of δ-Bi$_2$O$_3$ oxide ion conductors. I. The structure of (Bi$_2$O$_3$)$_{1-x}$(Y$_2$O$_3$)$_x$ as a function of x and temperature. J. Solid State Chem. 1986;63(1):8–15. https://doi.org/10.1016/0022-4596(86)90146-5.

7. Liu X, Abrahams I, Hull S, Norberg ST, Holdynski M, Krok F. A neutron total scattering study of defect structure in Bi$_3$Nb$_{0.5}$Y$_{0.5}$O$_{6.5}$. Solid State Ionics. 2011;192(1):176–180. https://doi.org/10.1016/j.ssi.2010.07.018.

8. Abrahams I, Liu X, Hull S, Norberg ST, Krok F, Szmigiel-Kozanecka A, Islam MS, Stokes SJ. A combined total scattering and simulation approach to analyzing defect structure in Bi$_3$YO$_6$. Chem. Mater. 2010;22(15):4435–4445. https://doi.org/10.1021/cm101130a.

9. Borowska-Centkowska A, Liu X, Krynski M, Leszczynska M, Wrobel W, Malys M, Hull S, Norberg ST, Krok F, Abrahams I. Defect structure in δ-Bi$_5$PbY$_2$O$_{11.5}$. RSC Adv. 2019;9(17):9640–9653. https://doi.org/10.1039/C9RA01233H.

10. Stambouli AB, Traversa E. Solid oxide fuel cells (SOFCs): A review of an environmentally clean and efficient source of energy. Renew. Sustain. Energy Rev. 2002;6(5):433–455. https://doi.org/10.1016/S1364-0321(02)00014-X.

11. Ruiz-Morales JC, Marrero-Lopez D, Galvez-Sanchez M, Canales-Vazquez J, Savaniu C, Savvin SN. Engineering of materials for solid oxide fuel cells and other energy and environmental applications. Energy Environ. Sci. 2010;3(11):1670–1681. https://doi.org/10.1039/C0EE00166J.

12. Zuo C, Liu M, Liu M. Solid Oxide Fuel Cells, in *Sol–gel Processing for Conventional and Alternative Energy*, (M. Aparicio, A. Jitianu, L. C. Klein eds.), vol. 5, 1st edn., Springer, New York, USA, 2012, pp. 7-37.

13. Haile SM. Fuel cell materials and components. Acta Mater. 2003;51(19):5981–6000. https://doi.org/10.1016/j.actamat.2003.08.004.

14. Fergus JW. Electrolytes for solid oxide fuel cells. J. Power Sources. 2006;162(1):30–40. https://doi.org/10.1016/j.jpowsour.2006.06.062.

15. Shuk P. Oxide ion conducting solid electrolytes based on Bi$_2$O$_3$. Solid State Ionics. 1996;89(3-4):179–196. https://doi.org/10.1016/0167-2738(96)00348-7.

16. Sammes NM, Tompsett GA, Näfe H, Aldinger F. Bismuth based oxide electrolytes— structure and ionic conductivity, J. Eur. Ceram. Soc. 1999;19(10):1801–1826. https://doi.org/10.1016/S0955-2219(99)00009-6.

17. Berezovsky J, Liu HK, Dou SX. Conductivity and microstructure of bismuth oxide-based electrolytes with enhanced stability. Solid State Ionics. 1993;66(3-4):201–206. https://doi.org/10.1016/0167-2738(93)90408-U.

18. Jiang N, Wachsman ED, Jung SH. A higher conductivity Bi$_2$O$_3$-based electrolyte. Solid State Ionics. 2002;150(3-4):347–353. https://doi.org/10.1016/S0167-2738(02)00291-6.

19. Kale KV, Jadhav KM, Bichile GK. Investigations on a high-conductivity solid electrolyte system, Bi$_2$O$_3$-Y$_2$O$_3$. J. Mater. Sci. Lett. 1999;18(1):9–11. https://doi.org/10.1023/A:1006652705028.

20. Takahashi T, Esaka T, Iwahara H. High oxide ion conduction in the sintered oxides of the system Bi$_2$O$_3$-Gd$_2$O$_3$. J. Appl. Electrochem. 1975;5(1):197–202. https://doi.org/10.1007/BF01637269.

21. Keizer K, Verkerk MJ, Burggraaf AJ. Preparation and properties of new oxygen ion conductors for use at low temperatures. Ceramurg. Int. 1979;5(4):143–147. https://doi.org/10.1016/0390-5519(79)90022-X.

22. Jung DW, Lee KT, Wachsman ED. Terbium and tungsten co-doped bismuth oxide electrolytes for low temperature solid oxide fuel cells. J. Korean Ceram. Soc. 2014;51(4):261–264. https://doi.org/10.4191/kcers.2014.51.4.260.

23. Verkerk MJ, Keizer K, Burggraaf AJ. High oxygen ion conduction in of the Bi$_2$O$_3$-Er$_2$O$_3$ system sintered oxides. J. Appl. Electrochem. 1980;10(1):81–90. https://doi.org/10.1007/BF00937342.

24. Takahashi T, Iwahara H, Arao T. High Oxide Ion Conduction in Sintered Oxides of the System Bi$_2$O$_3$-Y$_2$O$_3$. J. Appl. Electrochem. 1975;5(1):187–195. https://doi.org/10.1007/BF01637268.

25. Wang C, Xu X, Li B. Ionic and electronic conduction of oxygen ion conductors in the Bi$_2$O$_3$-Y$_2$O$_3$ system. Solid State Ionics. 1984;13(2):135–140. https://doi.org/10.7498/aps.33.221.

26. Lee JG, Kim SH, Yoon HH. Synthesis of yttria-doped bismuth oxide powder by carbonate coprecipitation for IT-SOFC electrolyte. J. Nanosci. Nanotechnol. 2011;11(1):820–823. https://doi.org/10.1166/jnn.2011.3199.

27. Wang SF, Hsu YF, Tsai WC, Lu HC. The phase stability and electrical conductivity of Bi$_2$O$_3$ ceramics stabilized by Co-dopants. J. Power Sources. 2012;218(1):106–112. https://doi.org/10.1016/j.jpowsour.2012.06.056.

28. Zhang XJ, Jin WT, Hao SJ, Zhao Y, Zhang H. Study of the crystal structures of new buffer materials Bi$_{1-x}$Y$_x$O$_{1.5}$. J. Supercond. Nov. Magn. 2010;23(1):1011–1014. https://doi.org/10.1007/s10948-009-0615-1.

29. Wu YC, Chang YW, Wang SF. Electrical properties and microstructural analysis of aliovalent-ion (Y^{3+}, Nb^{5+})-doped bismuth-based solid-oxide electrolyte. Ferroelectrics. 2013;455(1):123–128. https://doi.org/10.1080/00150193.2013.845486.

30. Liu X, Staubitz A, Gesing TM. Thermochromic Behavior of Yttrium-Substituted Bismuth Oxides. ACS Appl. Mater. Interfaces. 2019;11(36):33147–33156. https://doi.org/10.1021/acsami.9b11450.

31. Danks AE, Hall SR, Schnepp Z. The evolution of 'sol–gel' chemistry as a technique for materials synthesis. Mater. Horizons. 2016;3(2):91–112. https://doi.org/10.1039/C5MH00260E.

32. Grazulis S, Chateigner D, Downs RT, Yokochi AFT, Quiros M, Lutterotti L, Manakova E, Butkus J, Moeck P, Le Bail A. Crystallography Open Database - An open-access collection of crystal structures. J. Appl. Crystallogr. 2009;42(4):726–729. https://doi.org/10.1107/s0021889809016690.

33. Coelho AA. TOPAS and TOPAS-Academic: An optimization program integrating computer algebra and crystallographic objects written in C++. J. Appl. Crystallogr. 2018;51(1):210–218. https://doi.org/10.1107/S1600576718000183.

34. Dinnebier RE, Leineweber A, Evans JSO, eds., *Rietveld Refinement Practical Powder Diffraction Pattern Analysis Using Topas*, vol. 1, 1st edn., Walter de Gruyter GmbH, Berlin/Boston, 2019, pp. 16-129.

35. Cheary RW, Coelho AA, Cline JP. Fundamental parameters line profile fitting in laboratory diffractometers. J. Res. Natl. Inst. Stand. Technol. 2004;109(1):1–25. https://doi.org/10.6028/jres.109.002.

36. Cheary RW, Coelho AA. Axial Divergence in a Conventional X-ray Powder Diffractometer. I. Theoretical Foundations. J. Appl. Crystallogr. 1998;31(1):851–861. https://doi.org/10.1107/S0021889898006876.

37. Thompson P, Cox DE, Hastings JB. Rietveld Refinement of Debye-Scherrer Synchrotron X-ray Data from Al$_2$O$_3$. J. Appl. Crystallogr. 1987;20(1):79–83. https://doi.org/10.1107/S0021889887087090.

38. Hardcastle FD, Wachs IE. The molecular structure of bismuth oxide by Raman spectroscopy. J. Solid State Chem. 1992;97(2):319–331. https://doi.org/10.1016/0022-4596(92)90040-3.

39. de los Reyes M, Whittle KR, Zhang Z, Ashbrook SE, Mitchell MR, Jang L, Lumpkin GR. The pyrochlore to defect fluorite phase transition in Y$_2$Sn$_{2-x}$Zr$_x$O$_7$. RSC Adv. 2013;3(15):5090-5099. https://doi.org/10.1039/C3RA22704A.

40. Rubbens A, Drache M, Roussel P, Wignacourt JP. Raman scattering characterization of bismuth based mixed oxides with Bi$_2$O$_3$ related structures. Mater. Res. Bull. 2007;42(9):1683–1690. https://doi.org/10.1016/j.materresbull.2006.11.036.

41. Arasteh S, Maghsoudipour A, Alizadeh M, Nemati A. Effect of Y_2O_3 and Er_2O_3 co-dopants on phase stabilization of bismuth oxide. Ceram. Int. 2011;37(8):3451–3455. http://dx.doi.org/10.1016/j.ceramint.2011.04.136.

42. Denton AR, Ashcroft NW. Vegard's law. Phys. Rev. A. 1991;43(6):3161–3164. https://doi.org/10.1103/PhysRevA.43.3161.

43. Anilkumar M, Pasricha R, Ravi V. Synthesis of bismuth oxide nanoparticles by citrate gel method. Ceram. Int. 2005;31(1):889–891. https://doi.org/10.1016/J.CERAMINT.2004.09.002.

44. Tsuji K, Herisson De Beauvoir T, Ndayishimiye A, Wang K, Randall CA. Cold sintering of yttria-stabilized cubic bismuth oxide: Conductivity and microstructural evolution of metastable grain boundaries with annealing. J. Appl. Phys. 2020;128(21):215104-215104-8. https://doi.org/10.1063/5.0014287.

45. Jolley AG, Jayathilake R, Wachsman ED. Optimizing rhombohedral Bi_2O_3 conductivity for low temperature SOFC electrolytes. Ionics (Kiel). 2019;25(1):3531–3536. https://doi.org/10.1007/s11581-019-02920-x.

46. Takahashi T, Iwahara H, Nagai Y. High oxide ion conduction in sintered Bi_2O_3 containing SrO, CaO or La_2O_3. J. Appl. Electrochem. 1972;2(1):97–104. https://doi.org/10.1007/BF00609125.

47. Iwahara H, Esaka T, Sato T, Takahashi T. Formation of high oxide ion conductive phases in the sintered oxides of the system Bi_2O_3-Ln_2O_3 (Ln = La-Yb). J. Solid State Chem. 1981;39(2):173–180. https://doi.org/10.1016/0022-4596(81)90328-5.

48. Joshi AV, Kulkarni S, Nachlas J, Diamond J, Weber N. Phase stability and oxygen transport characteristics of yttria- and niobia-stabilized bismuth oxide. J. Mater. Sci. 1990;25(1):1237–1245. https://doi.org/10.1007/BF00585430.

49. Fung KZ, Virkar AV. Phase Stability, Phase Transformation Kinetics, and Conductivity of Y_2O_3-Bi_2O_3 Solid Electrolytes Containing Aliovalent Dopants. J. Am. Ceram. Soc. 1991;74(8):1970–1980. https://doi.org/10.1111/j.1151-2916.1991.tb07817.x.

50. Tietz F. Thermal expansion of SOFC materials. Ionics (Kiel). 1999;5(1):129–139. https://doi.org/10.1007/BF02375916.

51. Tietz F. Innovative materials in advanced energy technologies, in Proc. 9th CIMTEC - World Ceramic Congress and Forum on New Materials, (P. Vincenzini, ed.), vol. 24, Techna Publishers S.r.l., Faenza, Italy, 1999, pp. 61.

52. Jung HJ, Chung SY. Absence of distinctively high grain-boundary impedance in polycrystalline cubic bismuth oxide. J. Korean Ceram. Soc. 2017;54(5):413–421. http://dx.doi.org/10.4191/kcers.2017.54.5.06.

53. Meng G, Zhou M, Peng D. A new phenomenon - the inductive impedance in Bi_2O_3 based oxygen ionic conductors. Solid State Ionics. 1986;18-19(2):756–760. https://doi.org/10.1016/0167-2738(86)90257-2.

54. Harwig HA, Gerards AG. Electrical properties of the α, β, γ, and δ phases of bismuth sesquioxide. J. Solid State Chem. 1978;26(3):265–274. https://doi.org/10.1016/0022-4596(78)90161-5.

55. Changzhen W, Xiuguang X, Baozhen L. Ionic and electronic conduction of oxygen ion conductors in the Bi_2O_3-Y_2O_3 system. Solid State Ionics. 1984;13(2):135–140. https://doi.org/10.1016/0167-2738(84)90047-X.

56. Badwal SPS, Ciacchi FT. Oxygen-ion conducting electrolyte materials for solid oxide fuel cells. Ionics (Kiel). 2000;6(1):1–21. https://doi.org/10.1007/BF02375543.